

An Evaluation of Mesoscale Model Predictions of Down-Valley and Canyon Flows and Their Consequences Using Doppler Lidar Measurements during VTMX 2000

JEROME D. FAST

Pacific Northwest National Laboratory, Richland, Washington

LISA S. DARBY

NOAA/Environmental Technology Laboratory, Boulder, Colorado

(Manuscript received 3 July 2003, in final form 23 October 2003)

ABSTRACT

A mesoscale model, a Lagrangian particle dispersion model, and extensive Doppler lidar wind measurements during the Vertical Transport and Mixing (VTMX) 2000 field campaign were used to examine converging flows over the Salt Lake valley in Utah and their effect on vertical mixing at night and during the morning transition period. The simulated wind components were transformed into radial velocities to make a direct comparison with about 1.3 million Doppler lidar data points and to evaluate critically the spatial variations in the simulated wind fields aloft. The mesoscale model captured reasonably well the general features of the observed circulations, including the daytime up-valley flow; the nighttime slope, canyon, and down-valley flows; and the convergence of the flows over the valley. When there were errors in the simulated wind fields, they were usually associated with the timing, structure, or strength of specific flows. The simulated flow reversal during the evening transition period produced ascending motions over much of the valley atmosphere in the absence of significant ambient winds. Valley-mean vertical velocities became nearly zero as down-valley flow developed, but vertical velocities between 5 and 15 cm s⁻¹ occurred where downslope, canyon, and down-valley flows converged, and vertical velocities greater than 50 cm s⁻¹ were produced by hydraulic jumps. A fraction of tracer released at the surface was transported up to the height of the surrounding mountains; however, higher concentrations were produced aloft for evenings characterized by well-developed drainage circulations. Simulations with and without vertical motions in the particle model produced large differences in the tracer concentrations at specific locations and times, but the amount of tracer moving out of the valley atmosphere differed by only 5% or less. Despite the stability, turbulence produced by vertical wind shears mixed particles several hundred meters above the surface stable layer for the particle model simulation without vertical motions.

1. Introduction

Pollutants released within the stable boundary layer may remain highly concentrated because the strong atmospheric stability and weak turbulent motions limit the amount of vertical diffusion. Converging nocturnal drainage flows within closed basin topography exacerbate this problem by reducing horizontal advection. In converse, horizontal advection associated with drainage flows can be significant within open valley topography. The stable boundary layer over flat terrain is also largely decoupled from the ambient winds aloft. Less well known, however, is whether the mean vertical motions and shear generation of turbulence produced by converging nocturnal drainage flows within basin and valley atmospheres couple the stable boundary layer with the air aloft. These vertical exchange processes may sig-

nificantly enhance the dispersion of pollutants when compared with the stable boundary layer over flat terrain.

Our understanding of how various meteorological processes redistribute pollutants within basin and valley atmospheres has been limited by a lack of observations. Large cities usually have a number of monitoring stations that can be used to characterize the thermally driven slope and valley circulations at the surface, but the twice-daily rawinsonde network provides the only routine measurements aloft of the boundary layer and the free atmosphere. Field campaigns have been conducted that supplemented routine measurements with additional in situ and remote sensing instrumentation. These field campaigns have relied on point measurements, such as soundings, tethered balloons, sodars, and radar wind profilers.

Because the dynamic and thermodynamic structure of the atmosphere can be complex over basins and valleys, these point measurements are not necessarily spatially representative. Doppler lidars are increasingly being

Corresponding author address: Dr. Jerome D. Fast, Pacific Northwest National Laboratory, P.O. Box 999, K9-30, Richland, WA 99352.
E-mail: jerome.fast@pnl.gov

used to obtain high spatial and temporal resolution to fill in the information gap between the point measurements. For example, a Doppler lidar has been used to examine the evolution of thermally driven winds in the lower Fraser Valley in British Columbia, Canada (Banta et al. 1997), narrow jets exiting canyons along the Front Range of Colorado (Banta et al. 1995), and flow reversal within and above the Grand Canyon (Banta et al. 1999). Circulations observed aloft by lidars are often very different than measurements at the surface, indicating the presence of large vertical wind shears and vertical decoupling of the atmosphere.

Mesoscale models have also been used in conjunction with field-campaign measurements to improve the understanding of atmospheric processes in basins and valleys. Predicted wind fields have been compared with lidar scans (Clark et al. 2000; Darby et al. 2002; Fast 1995; Flamant et al. 2002; Reitebuch et al. 2003) and Doppler radar (e.g., Colle and Mass 1996), but these comparisons are usually only qualitative evaluations at select periods during the simulation period. Despite the large amount of data collected by lidars during field campaigns, modelers have utilized only a small fraction of this data. As far as we know, mesoscale model predictions have not been quantitatively evaluated using Doppler lidar measurements.

In this study, a mesoscale model and the extensive Doppler lidar measurements during the Vertical Transport and Mixing (VTMX) field campaign are used to examine the convergence and divergence patterns in the Salt Lake valley of Utah that are associated with the reversal of up-valley (northerly) and down-valley (southerly) flows during the evening transition period and well-developed down-valley and canyon flows at night. A unique aspect of this study is that radial velocity components are derived from the mesoscale model output so that a direct quantitative comparison can be made between the predicted spatial wind field and the Doppler lidar measurements. Nearly all of the lidar measurements are employed. After the predicted valley circulations have been evaluated, the consequences of the converging flows, including mean vertical motions and the effect of vertical mixing processes on ventilation, are presented.

2. VTMX field campaign

The VTMX field campaign, sponsored by the U.S. Department of Energy (DOE) Atmospheric Sciences Program, was conducted in the Salt Lake valley during October of 2000 (Doran et al. 2002). One of the objectives of the field campaign was to improve the understanding of meteorological processes responsible for the vertical transport and mixing of heat, momentum, and air pollutants during stable conditions. A wide range of remote sensing and in situ measurements were made. Measurements from the National Oceanic and Atmospheric Administration (NOAA)/Environmental Tech-

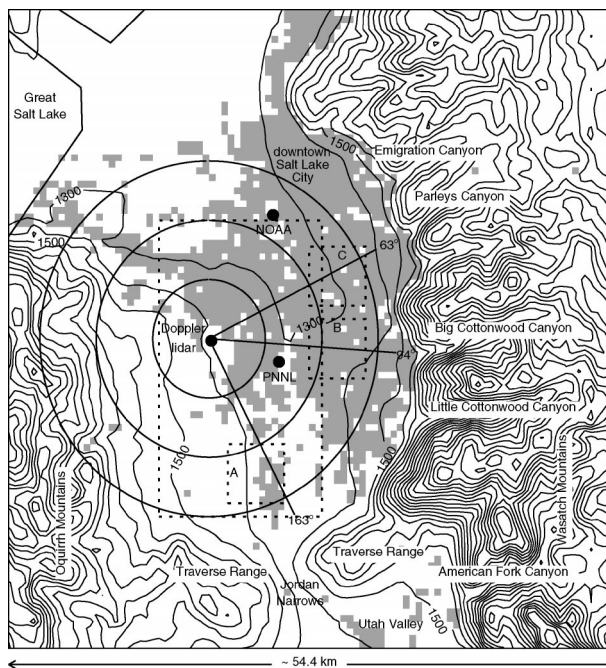


FIG. 1. Topography (100-m contour interval) and commercial and residential urban areas (shading) from RAMS grid 5 along with place names, location of the Doppler lidar, locations of the 63°, 94°, and 163° RHI scans, and locations of the NOAA and PNNL radar wind profilers used in the study. The concentric circles denote distances of 5, 10, and 15 km from the lidar, small boxes A, B, and C indicate subregions used to compare the observed and simulated radial velocities, and the large box denotes the subregion used to compute average simulated vertical velocities.

nology Laboratory scanning carbon dioxide Doppler lidar and the radar wind profilers operated by NOAA/Air Resources Laboratory and Pacific Northwest National Laboratory (PNNL) are employed by this study to examine convergence of down-valley and canyon flows at night. The locations of these instrumentation sites are shown in Fig. 1.

Much of the VTMX instrumentation operated continuously during the month, but the rawinsondes, tethered balloons, and lidars were only operated during intensive observational periods (IOPs). Ten IOPs were conducted during nocturnal stable periods and the morning and evening transition periods. Each IOP began in the late afternoon at 1500 LST (2200 UTC) and ended the following morning at 0900 LST (1600 UTC).

Data from eight IOPs (2, 3, 4, 5, 6, 7, 8, and 10) are employed in this study. IOPs 1 and 9 are not examined because some of the operational instrumentation was not deployed at the beginning of the field campaign for IOP 1 and because the Doppler lidar did not operate during IOP 9 because of the IOP's focus on measurements in the downtown area. Doran et al. (2002) grouped the IOPs into two categories: 1) those with well-developed drainage circulations and weak synoptic forcing (IOPs 5, 6, and 8), and 2) those with drainage circulations that were influenced for a period of time by

synoptic and mesoscale systems (IOPs 2, 3, 4, 7, and 10). In this study, we further divide category 2 into IOPs with and without downslope windstorms, because the valley circulations were very different for the windstorm events with easterly flow at ridge-top level.

The near-surface winds during IOPs 5 (14–15 October), 6 (16–17 October), and 8 (19–20 October) were characterized by downslope, down-valley, and canyon drainage flows during the entire evening, with light and variable winds a few hundred meters above the ground. Well-developed drainage circulations were observed prior to 0500 LST during IOPs 4 (8–9 October) and 7 (17–18 October), but the nocturnal inversions were eroded by southerly winds associated with approaching upper-level troughs. Southerly synoptic winds of greater than 10 m s^{-1} suppressed or significantly modified the local drainage circulations throughout IOP 10 (25–26 October). During IOP 2 (6–7 October), easterly downslope windstorms developed through the gaps of the Wasatch Mountains and spilled into the Salt Lake valley as a result of a cold air mass east of the Continental Divide that slowly progressed westward (Holland 2002). The strong winds channeled through the canyons persisted the following day through IOP 3 (7–8 October).

Although the radiosondes, sodars, and radar wind profilers provided vertical profiles of wind speed and direction that characterized the thermally driven circulations, the point observations do not provide detailed information on the spatial extent of the down-valley and canyon flows. The Doppler lidar, however, measured the spatial wind patterns over a large fraction of the valley atmosphere.

As described by Banta et al. (2003, manuscript submitted to *J. Appl. Meteor.*, hereinafter BAN03), the lidar was deployed on the western slope of the Salt Lake valley 5 km west of the valley center (Fig. 1). A series of scans with a range resolution of 300 m were completed during each IOP for constant elevation angles of 0.5° , 1.0° , 1.5° , 2.0° , 2.5° , and 3.0° , as depicted in Fig.

2a. These scans were made for all azimuth angles around the lidar, except for the 0.5° and 1.0° constant-elevation scans, which were made only between the 29° and 188° azimuth angles because of blocking of the lidar beam by the terrain west of the lidar. Each scan was completed in about 2 min. The height of the constant-elevation scan above the ground varied as a result of the topography. An example of the 3.0° constant-elevation scan is shown in Fig. 2b in which data 5 km from the lidar were 200 m above ground level (AGL). Constant-azimuth scans were made primarily at six angles, including 63° toward Parleys Canyon, 94° toward Big Cottonwood Canyon, and 163° toward the Jordan Narrows. Measurements for these scans were made up to an elevation angle of 45° to provide vertical profiles of the thermally driven canyon flows and pressure-driven flow through the terrain gap. Aerosols are the scattering targets for the lidar; therefore, the signal strength depends on the aerosol concentration, chemical composition, index of refraction of particles, relative humidity, and the absolute humidity. Data were usually obtained up to 15 km from the lidar, but data were occasionally obtained up to a range of only 5–10 km during periods of clean air. Radial velocities associated with low backscatter (i.e. low signal-to-noise ratio) were eliminated. The accuracy of the radial velocities measured by the lidar is 0.6 m s^{-1} .

Radial wind velocities toward and away from the lidar were obtained that can be used to determine the spatial extent of the down-valley and canyon flows and where those flows converged. As will be shown later, complex spatial flow patterns were frequently observed.

3. Model description

Version 5 of the Regional Atmospheric Modeling System (RAMS) mesoscale model (Pielke et al. 1992) was run for 8 of the 10 VTMX IOPs to simulate the boundary layer structure and circulations in the valley.

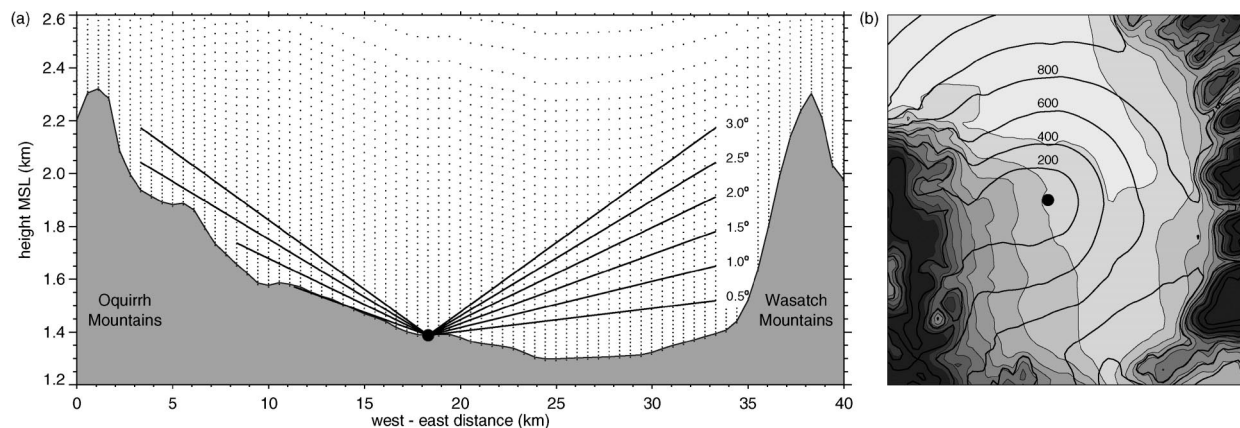


FIG. 2. (a) West-east vertical cross section through the lidar location that shows model grid coordinates (dots) and heights of the constant-elevation scans (lines), and (b) topography (shading) and height above ground level of the lidar 3.0° constant-elevation scan (200-m contour interval).

Five two-way interactive nested grids were used with grid spacings of 45, 15, 5, 1.7, and 0.56 km. The outer grid encompassed the western United States, and the inner grid encompassed the Salt Lake valley and the surrounding mountains and was the same size as the region shown in Fig. 1. The model employs a terrain-following vertical coordinate, and in this study the vertical grid spacing gradually increased from 15 m adjacent to the surface to 500 m near the model top at 14 km above sea level. About 40 grid points were located below the height of the mountains surrounding Salt Lake City, Utah.

The turbulence parameterization in the model consists of a simplified second-order closure method that employs a prognostic turbulence kinetic energy (TKE) equation (Mellor and Yamada 1982; Helfand and Labraga 1988). Cumulus and cloud microphysics parameterizations were not activated because of the mostly clear conditions observed during the VTMX IOPs; however, condensation to cloud water vapor was included. The shortwave and longwave parameterizations (Chen and Cotton 1983) take account of cloud effects to determine the heating or cooling caused by radiative flux divergences. Turbulent sensible heat, latent heat, and momentum fluxes in the surface layer were calculated from similarity equations. Prognostic soil-vegetation relationships were used to calculate the diurnal variations of temperature and moisture at the ground-atmosphere interface. For the outer grids, vegetation type was based on a 1-km U.S. Geological Survey (USGS) dataset; a more recent 100-m USGS dataset was used for the inner grid that had a more realistic distribution of urban land use.

Each of the simulations began at 0500 LST (1200 UTC) on the morning prior to an IOP and ended 36 h later at 1700 LST (0000 UTC) on the following day. Initial and boundary conditions were based on the National Centers for Environmental Prediction Global Forecast System model and operational upper-air soundings. The temperature of the Great Salt Lake was set to 14°C during the simulation period, based on the average observed value during October of 2000.

To facilitate a direct comparison of the predicted wind fields with the Doppler lidar data, radial velocities relative to the lidar location were obtained at each model grid point. The velocities were then interpolated vertically to correspond to the constant-elevation scans made by the lidar between 0.5° and 3.0°. Because the observed radial velocities were measured over an area that was about one-half of the size of the RAMS grid cell, the observed radial velocities were averaged over each model grid cell area for the statistical evaluations. It is desirable to have the predicted radial velocities equal to the observed values; however, the predicted wind fields are not evaluated fully because a particular observed radial velocity can be obtained with more than one wind direction. Nevertheless, this approach and the extensive lidar data provide a means of evaluating the

spatial wind field that cannot be obtained from any of the other instrumentation.

As discussed in section 4e, the Hybrid Particle and Concentration Transport (HYPART) model (Tremback et al. 1994) was used to simulate the effect of the nocturnal circulations on pollutant transport and mixing. Lagrangian particle dispersion was used to track a large number of particle positions, based on the mean velocity components produced by RAMS, and a subgrid-scale turbulent velocity component that is based on the predicted TKE fields.

4. Results

a. Overall model performance

An evaluation of the simulated winds, temperature, and humidity during IOPs 6, 7, and 10, using surface meteorological stations, radiosondes, and radar wind profilers, has been discussed by Zhong and Fast (2003). In this section, we present statistics that describe the model performance in simulating the winds measured by two radar wind profilers and the Doppler lidar.

Table 1 summarizes the mean bias (simulated – observed) and root-mean-square (rms) error in the predicted wind speed and direction over eight IOPs at the PNNL and NOAA radar wind profiler sites. For wind direction, negative and positive biases indicate a model error in the counterclockwise and clockwise directions, respectively. The results at every other range gate up to about 1.5 km AGL are shown. The wind speed bias at both sites was usually less than 1 m s⁻¹, with predicted wind speeds lower than observed at the PNNL site and higher than observed at the NOAA site. Rms errors were between 1.78 and 2.75 m s⁻¹ at the PNNL site and were between 2.66 and 3.30 m s⁻¹ at the NOAA site. The wind directions at both sites were more counterclockwise than observed (negative bias) and were usually within 10° within 1 km of the ground, indicating that the model down-valley winds had a more southeasterly component than the profiler data. Above 1 km, the wind directions were more clockwise (positive bias). The rms errors in wind direction were between 34.07° and 51.26° at the PNNL site and were between 36.20° and 52.74° at the NOAA site. In general, the rms errors in wind speed and direction were lower at the PNNL site than at the NOAA site. These statistics are similar to those described by Fast et al. (2002), using the RAMS model and radar wind profiler data in the vicinity of Philadelphia, Pennsylvania.

The large number of horizontal scans made by the Doppler lidar is a valuable resource that can be used to evaluate the predicted spatial variation of the winds over the valley. Correlation coefficients between the observed and simulated radial velocities are shown in Fig. 3 for constant elevation angles of 0.5°, 1.5°, and 3.0° during the eight IOPs, consisting of a total of 189, 184, and 176 scans, respectively. There were usually 150–

TABLE 1. Bias (simulated – observed) and rms of the predicted wind speed and direction at the NOAA and PNNL radar wind profiler sites for eight IOPs.

NOAA					PNNL				
Height (m AGL)	Speed		Direction		Height (m AGL)	Speed		Direction	
	Bias (m s ⁻¹)	Rms (m s ⁻¹)	Bias (°)	Rms (°)		Bias (m s ⁻¹)	Rms (m s ⁻¹)	Bias (°)	Rms (°)
124	-0.17	2.66	-2.45	36.20	110	-0.63	1.89	-0.49	34.07
234	0.20	2.73	0.32	39.00	220	0.04	1.78	0.36	32.72
344	0.05	2.70	-4.79	40.06	330	-0.14	1.94	-9.66	33.79
454	-0.01	2.92	-3.13	47.11	440	-0.72	1.99	-4.56	36.72
564	-0.56	3.23	-1.77	44.81	550	-0.43	1.91	-1.48	44.49
673	-0.09	3.03	-3.53	46.88	660	-0.03	1.73	-3.04	38.99
783	0.12	3.11	-14.06	50.80	770	-0.28	2.00	-4.86	38.22
838	0.50	3.38	-2.86	52.74	880	-0.78	2.26	4.60	41.93
948	0.73	3.27	2.35	54.15	990	-0.79	1.98	-6.46	49.57
1058	0.43	3.29	11.64	50.47	1100	-0.70	2.14	7.54	35.69
1168	0.63	2.90	15.47	50.90	1210	-0.41	2.37	10.53	38.73
1278	0.14	3.30	19.71	51.39	1320	-0.74	2.73	21.13	43.09
1388	0.71	3.09	11.92	47.45	1430	-1.24	2.75	22.18	51.26
1498	0.18	3.02	3.05	53.43	1540	-0.44	2.48	25.60	45.16

2000 pairs of observed and simulated values for each scan at a particular time, depending on the measurement range and the elevation angle. A correlation coefficient of 1.0 indicates that the simulated radial velocity pattern over the valley was identical to observed patterns. According to visual inspection of observed and simulated radial velocity plots, low correlation coefficients were obtained when the model reproduced the observed flow features in one area of the valley but not in another area.

In general, the correlation coefficients were higher

during periods of significant synoptic forcing. Correlation coefficients were usually greater than 0.9 and always greater than 0.75 throughout IOP 10, which was synoptically forced. When the synoptic southerly wind speeds increased during the latter parts of IOPs 4 and 7, correlation coefficients were greater than 0.75 as well. High correlation coefficients were also obtained for the daytime up-valley circulations that occurred until around sunset. The lowest correlation coefficients were obtained during the transition period between the af-

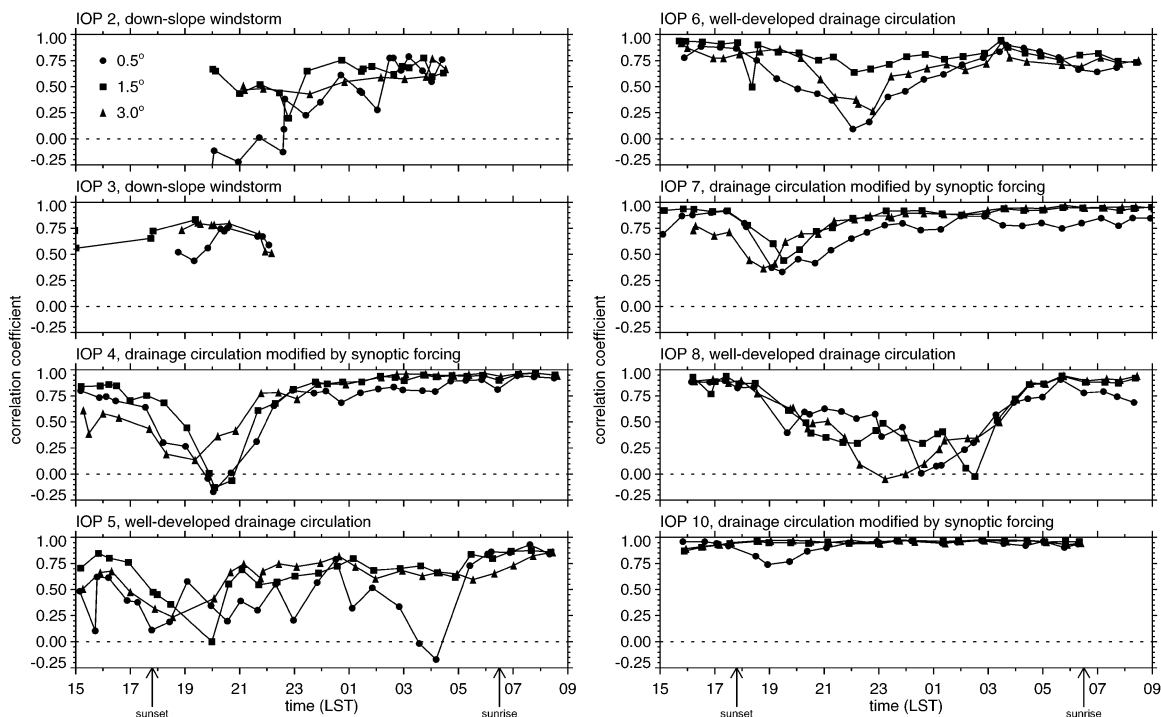


FIG. 3. Correlation coefficient between observed and simulated radial velocities as a function of time for 0.5°, 1.5°, and 3.0° constant-elevation scans for eight IOPs.

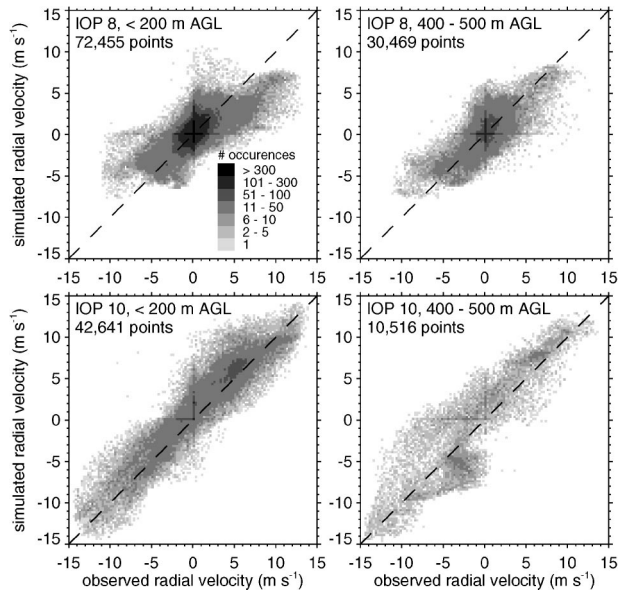


FIG. 4. Observed vs simulated radial velocities during IOP 8 and IOP 10 for two layers in the valley atmosphere.

ternoon up-valley flow and the development of the nocturnal drainage circulations. Low correlation coefficients were produced for only a few hours during the transition periods of IOPs 4, 6, and 7, but there were low values for several hours during IOP 8 because drainage flows did not become well developed until late in the evening. During IOP 5, low correlation coefficients persisted until shortly before sunrise, whereas the values aloft were usually greater than 0.6 after 2100 LST. The correlation coefficients were usually between 0.5 and 0.8 for the smaller number of scans available during the downslope windstorms of IOPs 2 and 3.

A plot of the observed and simulated radial velocities as a function of altitude for IOPs 8 and 10 is shown in Fig. 4. For the well-developed drainage flows during IOP 8, there was a large amount of scatter for those points within 200 m of the ground. There was less scatter aloft between 400 and 500 m AGL. In contrast, there was a much closer correspondence between the observed and simulated values both near the surface and aloft when strong southerly synoptic winds occurred during IOP 10, and there was much less variability in the winds across the valley.

b. Evolution of the valley circulations

As an example of a weak-ambient-flow case, the observed and predicted radial velocities along the 1.0° constant elevation angle at three times during IOP 8 is shown in Fig. 5. Thermally driven up-valley flow occurred in the late afternoon (Fig. 5a). The model results over most of the valley were consistent with the lidar measurements, with a correlation coefficient of 0.86. Beyond the range of the lidar, drainage flows were pre-

dicted to form shortly after sunset within all of the canyons along the Wasatch Mountains, consistent with surface measurements within these canyons (not shown). As the up-valley flow diminished, both the observations and simulation indicated that canyon and slope flows converged in the valley center (not shown). By 0230 LST, a down-valley jet formed over the southern valley with radial velocities as high as 6 m s^{-1} (Fig. 5b). The model, however, predicted that the drainage flows continued to converge over the valley center so that a low correlation coefficient of 0.05 was obtained. Correlation coefficients at other elevations were between -0.03 and 0.35 (Fig. 3). These low correlations can be attributed to a timing error in the initial development of the down-valley jet. A simulated down-valley jet slowly developed after 0230 LST so that by sunrise predicted winds over the valley were again consistent with the lidar measurements over a large fraction of the valley, producing a correlation coefficient of 0.80 (Fig. 5c). The spatial extent of the jet was similar to the one in the lidar scan, but the peak simulated radial velocities of approximately 7 m s^{-1} were lower than the peak observed values of 12 m s^{-1} over the southern valley. Both the measurements and the model showed that flows exiting Parleys Canyon and Big Cottonwood Canyon propagated over the valley and converged with the down-valley flow 5–8 km east of the lidar.

The simulated down-valley jet during IOP 8 and other IOPs formed as drainage flows converged in the Utah valley and spilled across the Traverse Range. The gap in the Traverse Range accelerated the flow, producing a wind maximum at the Jordan Narrows within 250 m of the ground. The predicted wind speed maximum was similar to the wind profiles measured by soundings at this location (Zhong and Fast 2003), although the vertical extent of the simulated jet was somewhat broader than was observed. The model also predicted higher wind speeds through the smaller gaps in the Traverse Range to the east and west of the Jordan Narrows (Fig. 5c). Although the range of the lidar measurements did not extend that far, there was some evidence of these flows propagating over the southern Salt Lake valley. The higher wind speeds over the eastern terrain gap in the Traverse Range resulted from a portion of the simulated drainage flow from American Fork Canyon that remained elevated over the Utah valley.

To illustrate the vertical structure of the valley winds during IOP 8, the observed radial velocities from the 163° constant-azimuth scan averaged between 7 and 9 km southeast of the lidar are shown in Fig. 6a along with the simulated values at the same location. The simulated down-valley flow within 200 m of the ground developed more slowly than did the winds measured by the lidar. Around sunrise, the simulated peak wind speeds were at 400 m AGL while the observed ones were at 100 m AGL. Differences in the radial components between 200 and 700 m AGL between 2000 and 0400 LST indicate wind direction errors in the middle-

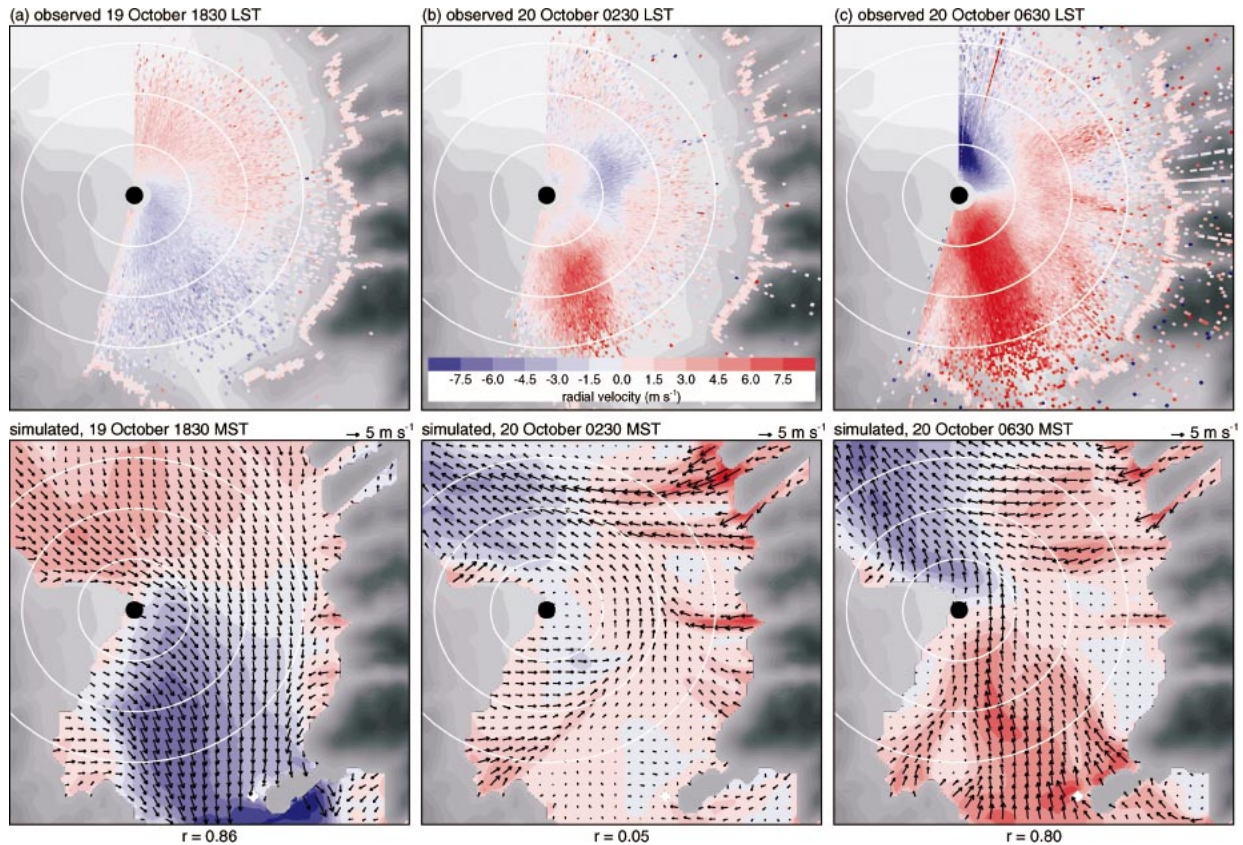


FIG. 5. Observed and simulated radial velocities along the 1.0° constant-elevation scan at (a) 1830, (b) 0230, and (c) 0630 LST representing up-valley, transition, and down-valley periods, respectively, during IOP 8. Red shading indicates flow toward the lidar site; blue shading indicates flow away from the lidar.

valley atmosphere as well. Both the observed and simulated winds above the height of the surrounding mountains were northerly, but the simulated radial velocities were one-half of the observed values.

Vertical profiles of the observed and simulated winds

during IOP 7 are shown in Fig. 6b to depict the effect of synoptic forcing on the valley circulation. Although the observed and simulated winds aloft were similar during IOP 7, the simulated northerly up-valley winds within 500 m of the ground around sunset were weaker

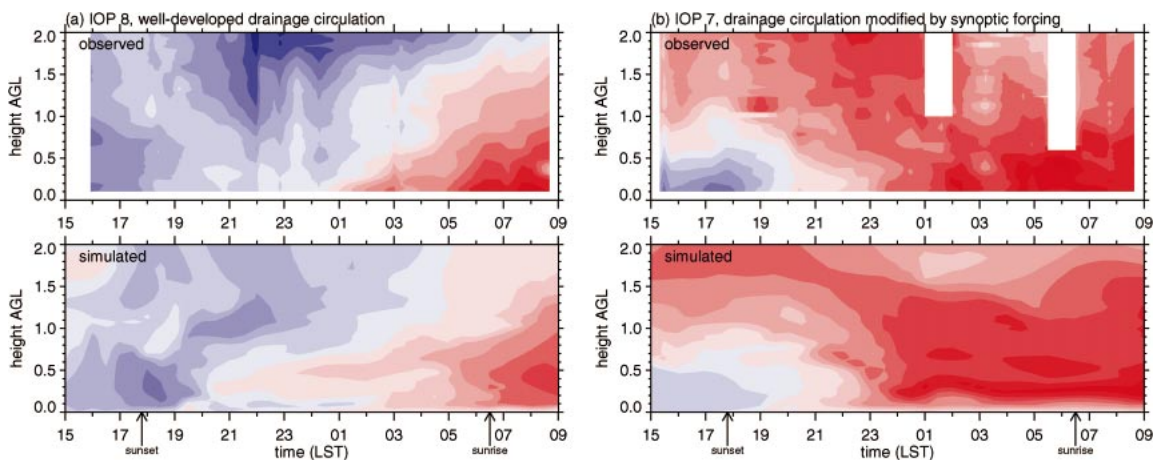


FIG. 6. Time–height plot of observed and predicted radial velocities along the 163° constant azimuth angle averaged between 7 and 9 km from the lidar for (a) IOP 8, characterized by well-developed drainage circulation, and (b) IOP 7, characterized by drainage circulation modified by synoptic forcing. Color scale is the same as in Fig. 5.

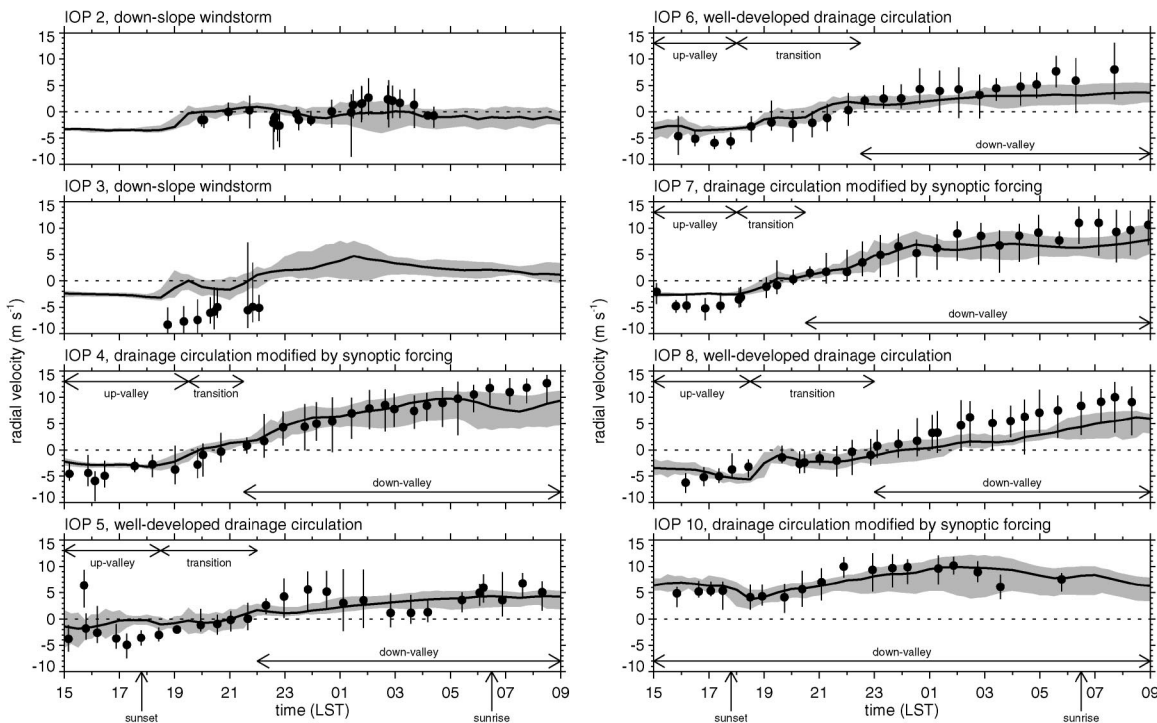


FIG. 7. Observed and simulated radial velocities along the 0.5° constant-elevation scan within sampling area A in Fig. 1, between 64 and 173 m AGL. Circles and vertical lines denote mean and range of the observed velocities, respectively. Thick line and gray shading denote mean and range of the simulated velocities, respectively. Positive and negative values indicate flow toward and away from the lidar, respectively.

than those observed. Down-valley flow near the surface started several hours earlier than it did during IOP 8. A southerly jet was simulated between 200 and 300 m AGL after midnight with winds speeds that increased to 11 m s⁻¹ by sunrise, but the lidar indicated that the jet was deeper and the wind speeds were more variable.

To evaluate the up-valley and down-valley flow close to the surface for all of the IOPs, the average and range of radial velocities that were observed and predicted along the 0.5° constant elevation angle within sampling area “A” (Fig. 1) are shown in Fig. 7.

In general, the simulated winds within sampling area A were usually consistent with the lidar observations. During IOP 10, which was synoptically forced, the positive (southerly) radial velocities throughout the period illustrate that southerly winds overwhelmed the afternoon thermally driven terrain forcing so that no flow reversal occurred. For the other IOPs, the magnitude of the afternoon up-valley flows was usually underestimated by 1–2 m s⁻¹. The largest difference occurred just before sunset during IOP 5 at which time the predicted radial velocities were nearly zero while the observations were 4–5 m s⁻¹. Visual inspection of horizontal plots similar to Fig. 5 revealed that this discrepancy was a wind direction error because the predicted winds of 3 m s⁻¹ were northeasterly, perpendicular to the radial component in this region.

The lidar data indicated that the time of flow reversal from up-valley to down-valley flow, as indicated by a

change in sign in the radial velocities, was well simulated within sampling area A during IOPs 4, 5, and 7. The simulated transition to southerly flow occurred 1 h too soon during IOP 6 and 2 h too late during IOP 8. During IOPs 4 and 7, the predicted increases in wind speed after midnight when the valley circulations were modified by synoptic forcing were consistent with the lidar measurements, but the speeds were lower than were observed after 0600 LST. About 100 m higher along the 1.0° constant-elevation-angle scan, the simulated speeds were much closer to the measurements (not shown). In contrast, the simulated increase in the down-valley wind speed was too low both near the surface and aloft (not shown) during the well-developed drainage circulations of IOPs 6 and 8.

During IOP 5, down-valley winds as high as 9 m s⁻¹ occurred around midnight, but the speeds dropped to nearly zero by 0400 LST before increasing to 9 m s⁻¹ again around sunrise. The model did not produce this behavior. Instead, the simulated down-valley wind speeds slowly increased with time, similar to the behavior observed in IOPs 6 and 8. BAN03 demonstrated that the timing of the flow reversal in the valley and the magnitude of the down-valley winds were related to the regional-scale pressure gradients, as determined between Pocatello, Idaho, and Price, Utah. They noted that during IOP 5 and, to a lesser extent, during IOP 6 the decrease in the down-valley wind speed corresponded to a decrease in the pressure difference between these

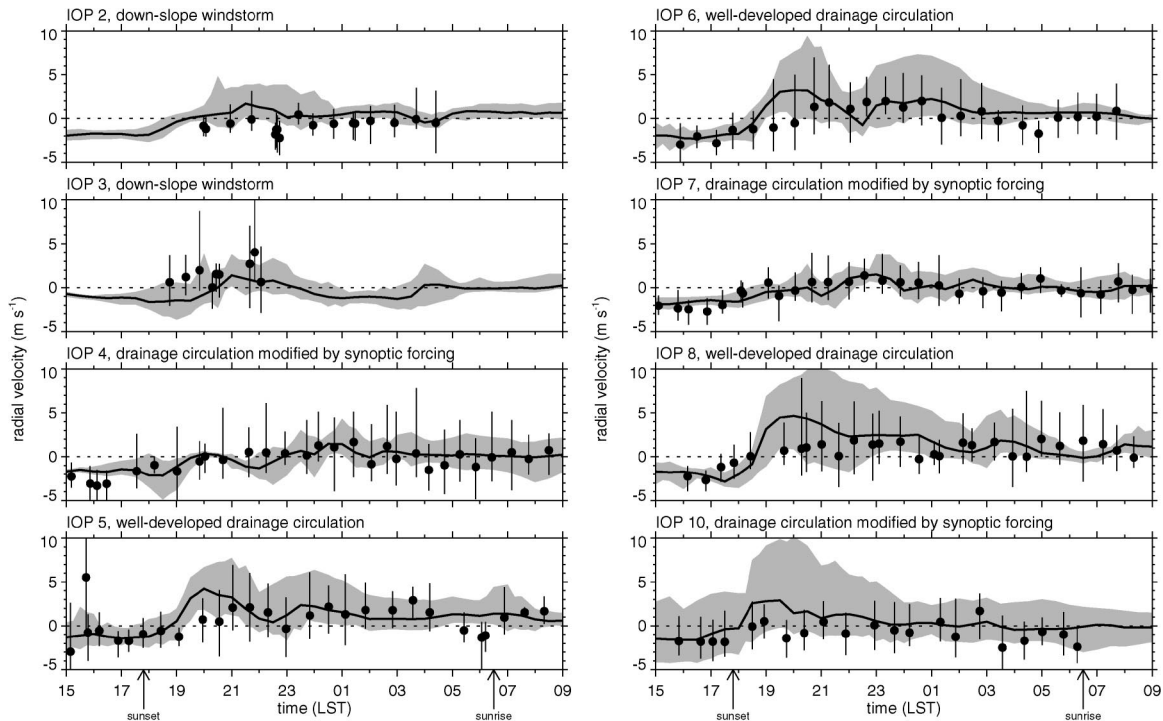


FIG. 8. Same as in Fig. 7, but for sampling area B between 81 and 185 m AGL west of Big Cottonwood Canyon. Canyon outflows are represented by positive values.

two sites. Reductions in the pressure difference did not occur during the other IOPs. The simulated pressure differences between Pocatello and Price were similar to those reported in BAN03, except that the model did not produce a decrease in the pressure difference during IOPs 5 and 6. Therefore, the errors in the magnitude of the down-valley flow associated with the low correlations in Fig. 3 are likely related to errors in the regional-scale pressure gradient.

The diurnal valley winds were disrupted by the down-slope windstorm during IOPs 2 and 3. While southerly down-valley flow was observed between 0100 and 0400 LST during IOP 2 the radial velocities were less than 5 m s^{-1} in sampling area A. The simulated winds were weaker and more variable. The available lidar scans during IOP 3 indicated that winds emanating from Parleys Canyon propagated across the valley and produced northerly winds in this region. The simulated northerly radial velocities were much lower than those observed because predicted downslope winds over the lower slopes of the Oquirrh Mountains converged with the canyon outflow.

Both the lidar data and the simulated winds indicated that the down-valley jet axis usually had a slight southeast–northwest orientation with peak speeds located just west of the valley center (e.g., Fig. 5c). Because a significant amount of spatial variability in the winds occurred near the PNNL site, the radar wind profiler data may not be representative of the valley circulation. The observed and simulated peak wind speeds at that lo-

cation (not shown) were usually lower than those from sampling area A because the jet axis was a few kilometers west of the PNNL site.

c. Evolution of the canyon flows

Surface measurements indicated that nocturnal wind speeds at the base of Parleys Canyon were frequently as high as 5 m s^{-1} ; however, the easterly drainage wind speeds at the base of Big and Little Cottonwood Canyons were usually light. Stations located a few kilometers west of the canyons usually did not show any evidence of canyon outflow. Only during the downslope windstorm events, when wind speeds at the base of Parleys Canyon reached 15 m s^{-1} , were the effects of the canyon outflow observed at other stations on the valley floor. The surface observations, however, were not representative of the flows aloft. During periods when light drainage winds were observed at the surface, the Doppler lidar often observed strong flows exiting all of these canyons. The spatial extent and magnitude varied significantly in time.

To illustrate the evolution of the winds from Big Cottonwood Canyon, the observed and simulated radial velocities along the 0.5° constant elevation angle within sampling area “B” (Fig. 1) are shown in Fig. 8. The largest canyon outflow was observed during well-developed drainage circulations of the weak ambient flow IOPs (5, 6, and 8). For these IOPs, radial wind speeds began to increase after sunset, becoming as high as 9

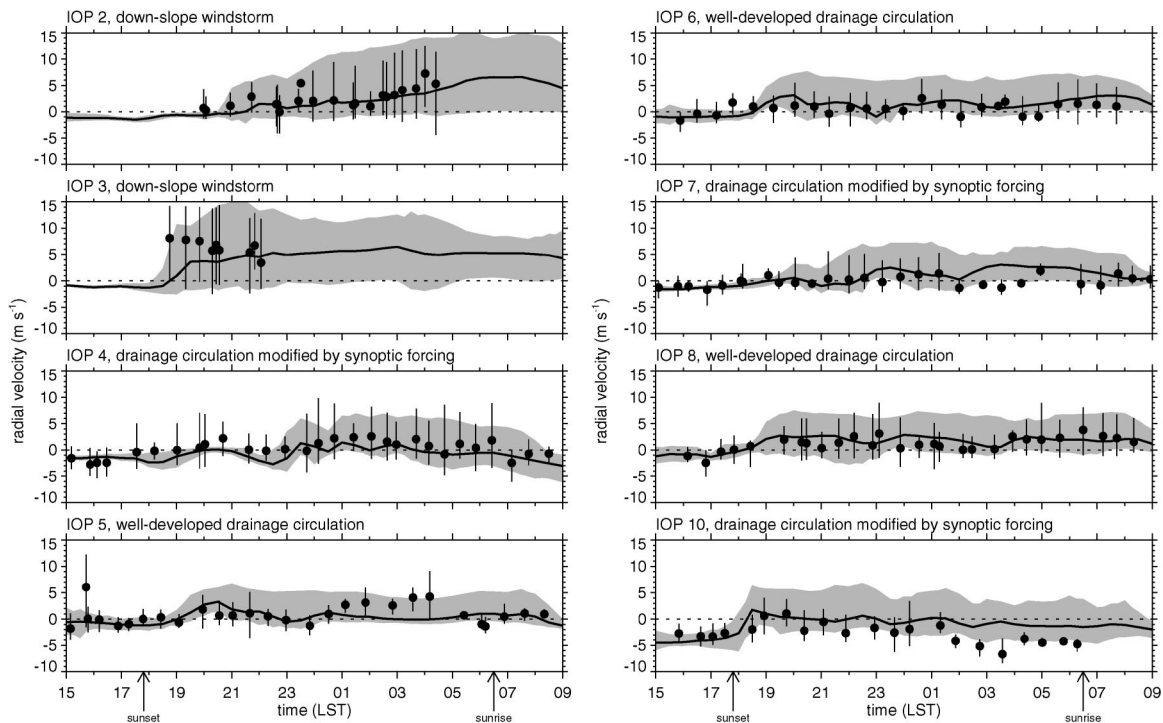


FIG. 9. Same as in Fig. 7, but for sampling area C between 171 and 192 m AGL southwest of Parleys Canyon.

m s^{-1} between 2000 and 2100 LST during IOP 8. The canyon outflow slowly diminished by sunrise so that the average radial velocities were nearly zero, and there were one or more peak values observed during the evening. During the synoptically modified periods of IOPs 4, 7, and 10, the winds exiting the canyon were generally weaker, although there were periods in which radial velocities were between 3 and 5 m s^{-1} during IOP 4. Note that some negative values were obtained in this box that indicate flow away from the lidar. This westerly flow toward the Wasatch Mountains resulted from horizontal eddies on either side of the easterly canyon outflow.

Many of the features of the radial velocities observed in sampling area B were reproduced by the model for all of the IOPs. Although the model predicted strong outflows exiting Big Cottonwood Canyon shortly after sunset, they developed approximately 1 h sooner than observed. The model also produced some of the temporal variability in the strength of the canyon outflow, especially during IOPs 5, 6, and 8. The observed and simulated mean radial velocities were similar during IOPs 4 and 7 when the synoptic forcing modified the drainage circulations; however, the range of simulated values was much less than was observed for IOP 4. A few hours before sunrise, during IOP 8, the simulated radial velocities were significantly lower than the observed values because the canyon outflow was predicted to occur at a higher altitude. The simulated radial velocities were closer to the lidar measurements 100 m higher, as shown by the results along the 1.0° constant-elevation-angle scan in Fig. 5. Some of the observed

and simulated negative radial velocities among the IOPs were indicative of horizontal eddies on either side of the outflow from Big Cottonwood Canyon, similar to those in Fig. 5c. During IOP 10, with the strongest synoptic forcing, the model produced strong outflow when none was observed between 1800 and 2300 LST. Part of this discrepancy may be due to the limited lidar range that reduced the number of data points to about one-third of what was obtained for other IOPs. In this case, the simulated canyon outflow may have just propagated too far over the valley floor, or there were a number of model grid cells within sampling area B that were beyond the range of the lidar.

In a similar way, Fig. 9 shows the behavior of the flow exiting Parleys Canyon within sampling area "C" (Fig. 1). Observed and simulated radial velocities toward the lidar were usually less than 5 m s^{-1} for both the well-developed drainage circulation periods (IOPs 5, 6, and 8) and the synoptically modified periods (IOPs 4 and 7). The time variation of the simulated average and range of values was similar to the observed values for many periods. During IOP 10, the lidar observed negative radial velocities, reflecting the strong southerly flow that is away from the lidar in this region. As with Big Cottonwood Canyon, the model overpredicted the strength of the flow exiting Parleys Canyon outflow for IOP 10. The highest positive radial velocities occurred during IOPs 2 and 3 for the downslope windstorm events. The simulated increase in magnitude and range radial velocities was similar to the observed values dur-

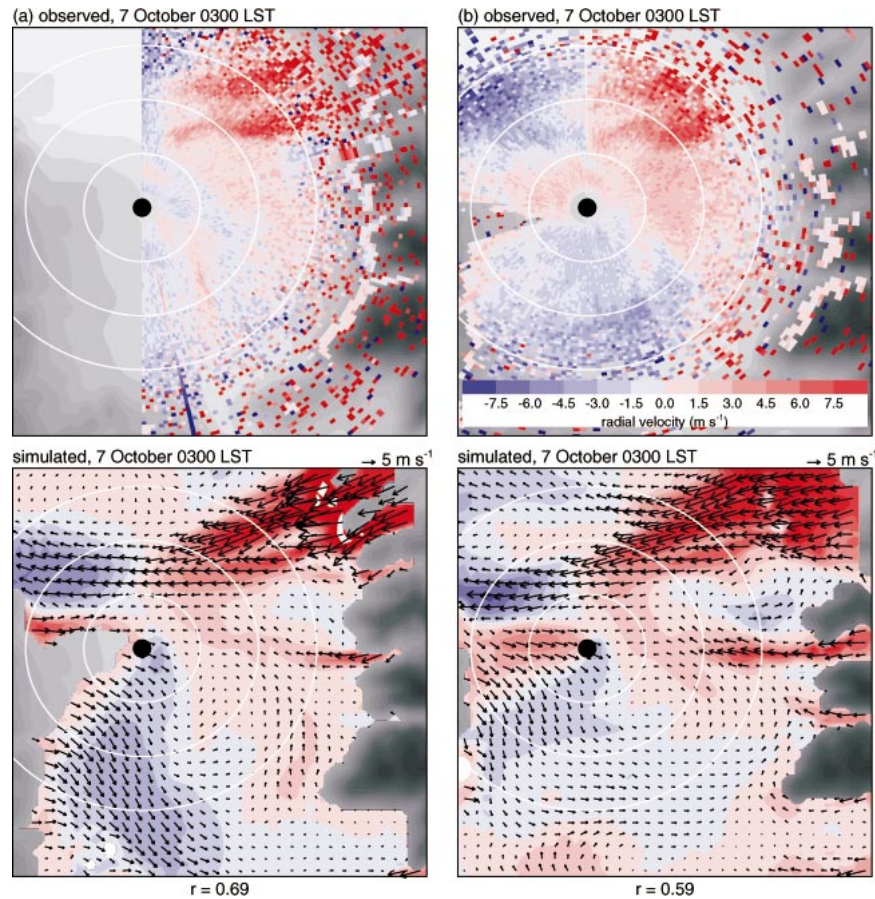


FIG. 10. Observed and simulated radial velocities along the (a) 1.5° and (b) 2.5° constant elevation angle at 0300 LST for the downslope windstorm during IOP 2.

ing IOP 2, but the simulated radial velocities just after sunset during IOP 3 were too low.

Figure 10 depicts the observed and simulated spatial extent of the canyon jets for the downslope windstorm during IOP 2 at 0300 LST. At all of the elevation angles, strong winds emanated through Emigration and Parleys Canyons that propagated to the west over the northern Salt Lake valley. At low elevation angles (Fig. 10a), the winds over the southern valley were light and variable, but northerly winds were observed over the southern valley at higher elevation angles (Fig. 10b). The simulated wind fields were similar to the lidar measurements and indicated that the strong canyon outflows lead to the formation of a large horizontal eddy circulation over the southern valley.

As indicated in Figs. 8 and 9, the canyon outflow wind speeds were variable during the evening. The lidar scans also showed that the canyon jets extended to the valley center at times and then retreated back to the base of the Wasatch Mountains. Convergence of the down-valley and canyon flows frequently occurred about 5 km northeast of the lidar, as shown in Fig. 5c.

A quantitative measure of the location where outflow from Parleys Canyon and Big Cottonwood Canyon out-

flow converged with the down-valley flow was obtained by determining the distance from the lidar along the 63° constant azimuth angle at which the radial velocities changed from negative to positive values along the 0.5° constant-elevation scans. The results are depicted in Fig. 11 along with the simulated values. At times, the extent of the canyon outflow could not be determined because negative radial velocities were beyond the maximum range of the lidar. In general, the convergence zone was located closer to the lidar during the well-developed drainage circulations of IOPs 5, 6, and 8 than during IOPs 4, 7, and 10, when the drainage circulations were modified by synoptic forcing. Changes in the convergence zone locations were simulated well for some evenings, such as IOP 8, but not for others. During IOP 6, Parleys Canyon outflow advanced rapidly to the valley center between 2100 and 2300 LST and then gradually retreated to 10 km northeast of the lidar as the down-valley flow intensified. The model predicted the initial advance of the canyon outflow, but then it remained about 5 km northeast of the lidar for the rest of the evening. During IOPs 4 and 7, prior to the onset of the strong southerly synoptic winds around 0500 LST, Parleys Canyon outflow was observed and predicted to ad-

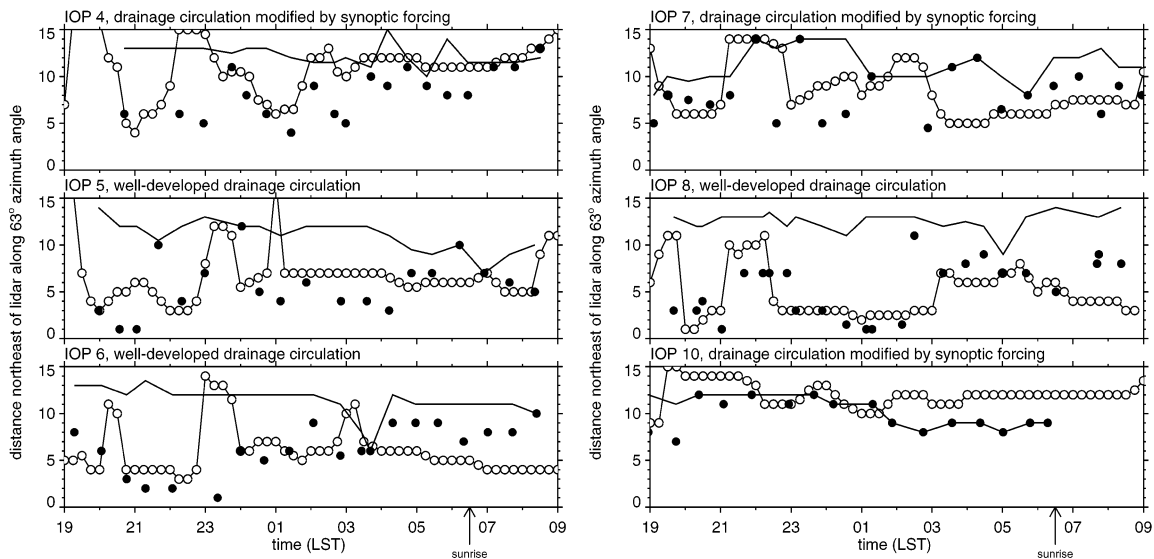


FIG. 11. Observed (filled circles) and simulated (open circles) distance northeast of the lidar along the 63.7° constant azimuth angle (Fig. 1) where convergence occurred. Line indicates the maximum range of lidar data.

vance and retreat two times, although the simulated values were out of phase with the observations. Among all of the IOPs, the observed and simulated convergence zone was the farthest away from the lidar during IOP 10, which had the strongest synoptic forcing.

d. Mean vertical velocities

In areas of relatively flat terrain, vertical velocities W are usually relatively small ($<1 \text{ cm s}^{-1}$) within the stable boundary layer and may not be very important in the vertical transport of pollutants. However, the converging slope, canyon, and down-valley flows in the Salt Lake valley, discussed previously, are likely to produce strong vertical motions. The simulated mean vertical velocity fields produced by convergence and divergence over the valley are likely to be realistic when the correlation coefficient between the observed and simulated radial velocities is high and when the simulated winds are consistent with the point measurements. In converse; the simulated vertical velocity fields are not likely to follow reality exactly over the entire valley atmosphere when the correlation coefficient is low; however, the vertical velocity fields may be realistic over a portion of the valley. Given that most of the differences between the lidar measurements and the model resulted from errors in the timing or spatial structure of specific flows, the peak rising and sinking motions would be displaced in space and time but would represent typical conditions within the valley atmosphere for the entire evening.

Examples of the predicted vertical velocities along the 1.0° constant-elevation-angle scans during a case of well-developed drainage circulations (IOP 8) are shown in Fig. 12. During the late afternoon and early evening,

the up-valley and upslope flows produced ascending motions over most of the region (not shown). As the canyon and drainage flows developed and converged west of the valley center at 2215 LST (Fig. 12a) strong descending motions occurred over the steep slopes and ascending motions occurred over a large fraction of the valley floor. Areas of ascending and descending vertical velocities as high as $6\text{--}12 \text{ cm s}^{-1}$ resulted from the strong wind shears associated with outflow from all of the canyons along the Wasatch Mountains. As the down-valley flow gradually developed after 0230 LST (Figs. 12b,c) a larger fraction of the valley atmosphere consisted of descending motions. Ascending vertical velocities in excess of 50 cm s^{-1} were produced by hydraulic jumps associated with the down-valley flow over the Traverse Range and the Parleys Canyon and Emigration Canyon outflows.

Although the vertical velocity distributions were complex, the overall valley-mean vertical motions were similar for IOPs in the same synoptic category. Figure 13 depicts the simulated vertical motions averaged over the large box shown in Fig. 1. For the well-developed drainage circulations during IOPs 5, 6, and 8, strong ascending motions within 0.6 km of the ground were produced during the 1800–2100 LST transition period. The average vertical velocities near the surface after 2100 LST were negative as a result of flows down the slopes and valley toward the lower elevations of the Great Salt Lake. During IOPs 4, 7, and 10 in which the drainage circulations were modified by synoptic forcing, the ascending motions during the transition period were greatly reduced or were eliminated entirely. In contrast with IOPs 5, 6, and 8, stronger positive and negative vertical motions were produced in the middle of the valley atmosphere after 2100 LST. Southerly flow occurred dur-

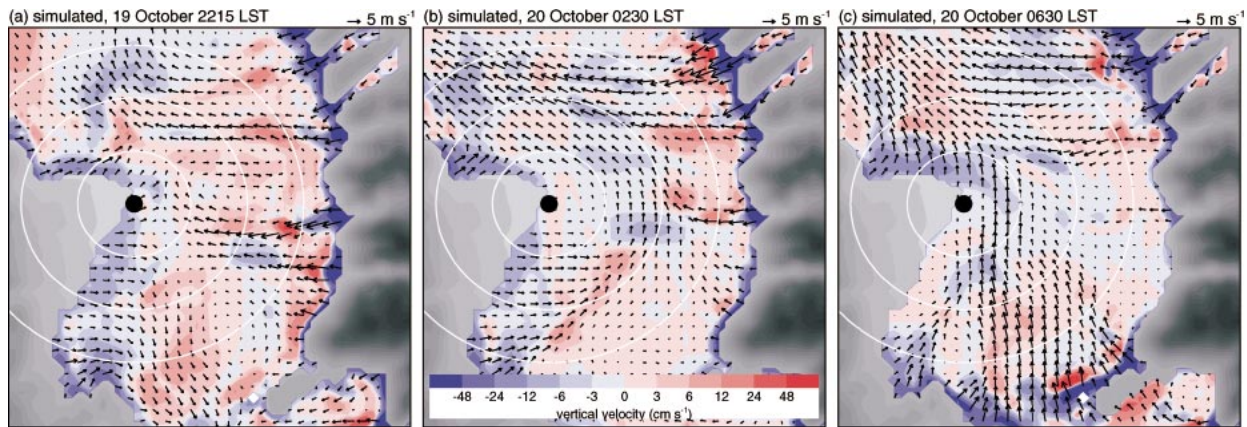


FIG. 12. Simulated vertical velocities along the 1.0° constant-elevation scan at (a) 2215, (b) 0230, and (c) 0630 LST during the up-valley, transition, and down-valley periods, respectively, during IOP 8, shown in Fig. 5. Red shading indicates upward vertical velocity, and blue shading represents downward vertical velocity.

ing the late evening of all three IOPs, but descending motions were produced during IOP 4, ascending motions were produced during IOP 7, and periods of both ascending and descending motions were produced during IOP 10. For the downslope windstorm events of IOPs 2 and 3, ascending motions were produced during most of the evening as a result of the easterly flow that produced large horizontal eddies over the entire valley.

e. Effect of converging flows on ventilation

The HYPACT model was used to examine the effect of mean vertical motions and turbulence associated with the converging flows on the transport and mixing of surface releases. Within the shaded region depicted in Fig. 14, simulated particles were released at a constant rate within 5 m of the ground from 1900 to 0700 LST. A total of 14 400 particles were released for each IOP. The fraction of particles remaining over the Salt Lake valley is shown in the right part of Fig. 14. Not surprising is that during IOPs 4, 7, and 10, with the strongest winds aloft, the percent of particles remaining over the valley quickly dropped to 35% or less in a few hours. The particle fraction leveled off between 0100 and 0700 LST because the particles gained by surface releases were offset by particles lost from horizontal transport toward the Great Salt Lake. After the end of the release period at 0700 LST, the particle fraction dropped to nearly zero 4 h after sunrise. Despite the predominant southerly flow within the valley, some particles remained over the eastern side of the valley because of the lighter winds in this region produced by the converging canyon and down-valley flows.

A larger fraction of the particles remained over the valley between 2300 and 0300 LST of IOPs 5, 6, and 8 because of variable winds during the transition period between the up-valley and down-valley circulations. However, as the down-valley jet developed by sunrise the particle fraction dropped to levels similar to those

from IOPs 4, 7, and 10. The stronger canyon outflows during these evenings permitted somewhat more particles to remain over the eastern valley after sunrise as indicated by the higher particle fractions after 0700 LST. The particle fraction for the downslope windstorm event during IOP 3 was similar to IOPs modified by synoptic forcing because the canyon outflow had an east–west orientation that permitted particles to be transported out of the valley. In contrast, IOP 2 had the highest number of particles remaining over the valley among all the simulation periods because the canyon outflow produced a horizontal eddy over much of the valley so that particles were trapped within the valley atmosphere.

The depth of vertical mixing of particles also varied among the IOPs, as indicated by the vertical profiles of the total number of particles within the sampling domain at 0700 LST (Fig. 15). During the downslope windstorm events of IOPs 2 and 3, more particles were located near the surface between 0.2 and 0.8 km AGL than during the other IOPs. IOPs 5, 6, and 8 had considerably higher particle numbers between 1 km AGL and above the average mountain peak heights. The mean vertical motions and/or turbulence associated with the converging drainage flows during these evenings were apparently large enough to transport material vertically out of the valley atmosphere more effectively than during the other IOPs.

The average vertical velocities near the surface were usually negative after 2100 LST (Fig. 13) as a result of southerly near-surface drainage flows down the valley slope. The horizontal variability of the vertical velocity fields was, in fact, complex (Fig. 12), with regions of strong positive and negative vertical velocities produced by the converging flows superimposed on the overall sinking associated with the near-surface drainage flows. To isolate the net effect of turbulent mixing on the particle distribution, the HYPACT simulations were repeated by setting the vertical velocities to zero.

The differences in the number of particles between

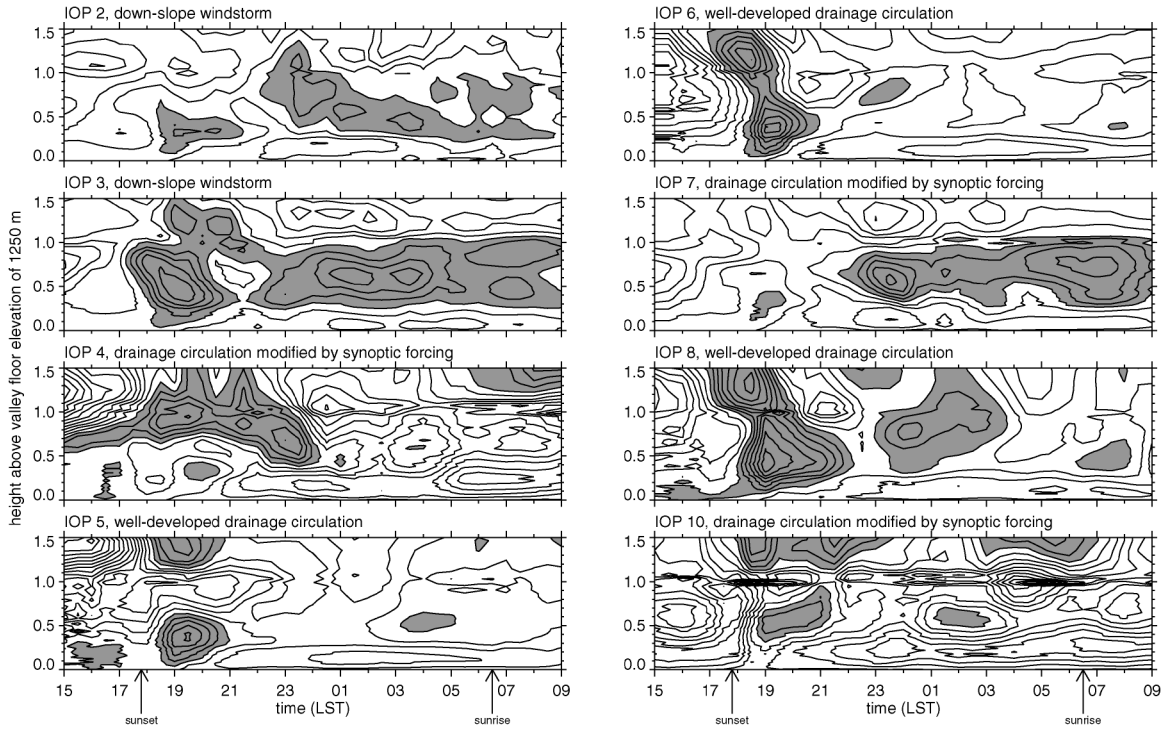


FIG. 13. Simulated average vertical velocities (contour interval of 1 cm s^{-1}) over the valley center as defined by the large dotted box in Fig. 1, where shading denotes positive values.

the simulations with and without vertical velocity at 0100 and 0700 LST are shown in Fig. 16. During the downslope windstorm events of IOPs 2 and 3, the simulation with mean vertical velocities set to zero retained more particles within 0.3 km of the ground. The large horizontal eddy (Fig. 10) produced positive vertical motions over much of the valley, although the average vertical velocities were slightly negative near the surface (Fig. 13). When these vertical velocities were set to zero, more particles remained near the surface so that fewer particles were transported upward to the 0.3–1.0-km layer above the valley floor. In contrast, more particles were

lost within 0.2 km of the ground for the well-developed drainage circulations during IOPs 5, 6, and 8, when the vertical velocity was set to zero. For these cases, sinking motions dominated the vertical advection over the valley (Fig. 13) so that particles were more likely to be trapped near the surface. When the vertical motions were set to zero, more particles were transported just above the surface stable layer by turbulent mixing. A similar result was produced for the drainage circulations modified by synoptic forcing during IOPs 4, 7, and 10, except that the net effect of the vertical motions was smaller. Although strong vertical motions were produced during

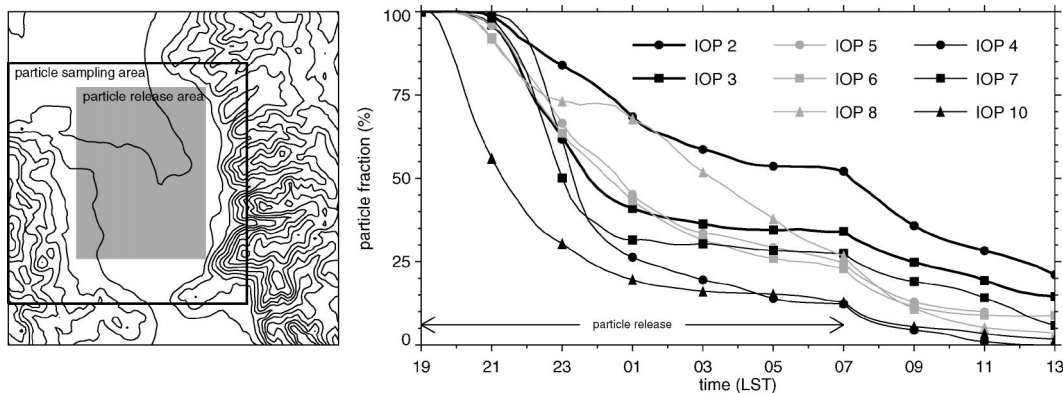


FIG. 14. Percent of particles released over the valley center (shading at left) at a constant rate between 1900 and 0700 LST remaining over the valley (box at left), as a function of time.

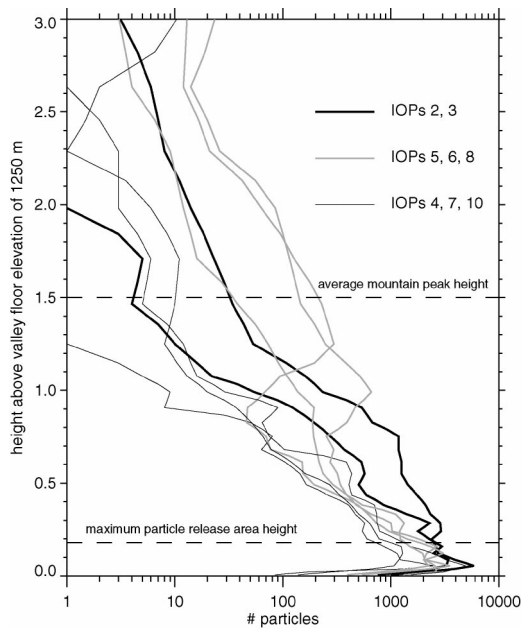


FIG. 15. Total number of particles within the sampling domain denoted in Fig. 14 at 0700 LST as a function of height above the valley floor.

these cases, the southerly ambient winds probably enhanced horizontal transport.

The fraction of particles remaining over the Salt Lake valley and vertical profiles of particles from the simulation without vertical velocities were very similar to those shown in Figs. 14 and 15. Eliminating vertical motions changed the particle fraction at any given time by only about 5%. Differences at specific locations and times were, however, large. This result implies that an accurate representation of the vertical motion fields within the stable boundary layer is needed to represent vertical mixing of point sources, such as those from industrial stacks, adequately.

The model results suggest that, although vertical motions modify the transport of material in the valley atmosphere, turbulence was more important. Even during the nocturnal stable conditions in the valley, turbulent motions transported a fraction of surface releases up to the height of the surrounding mountains. However, turbulence parameterizations in mesoscale models are known to be subject to large errors during stable conditions, and improving these parameterizations is still the subject of ongoing research (Doran et al., 2002). Fast and Shaw (2002) showed that the simulated TKE and dissipation rate during the VTMX IOPs was often

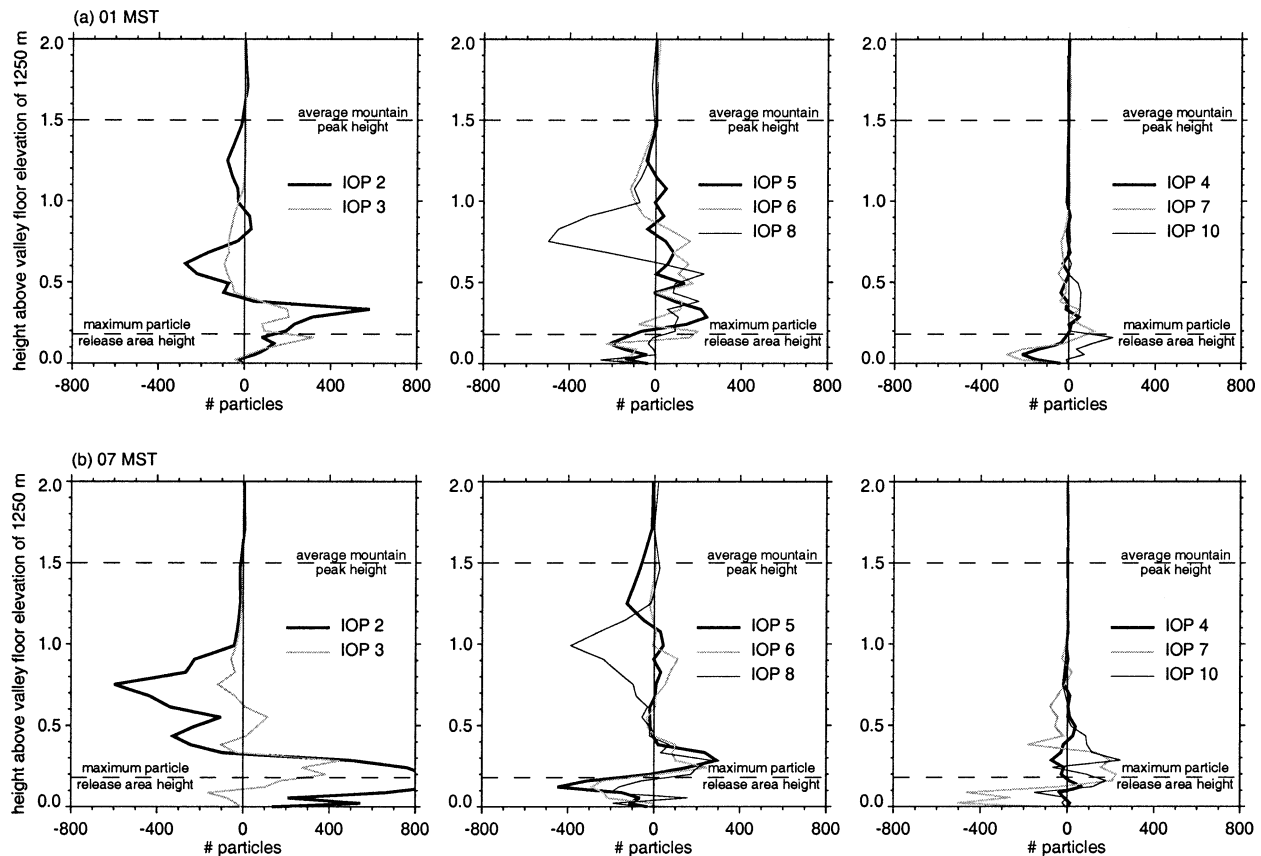


FIG. 16. Difference (simulation without w - simulation with w) in the number of particles within the sampling domain denoted in Fig. 14 at (a) 0100 and (b) 0700 LST.

underestimated aloft when compared with measurements obtained from a radar wind profiler and an aircraft. Therefore, the dispersion model may be underestimating the upward transport of material by turbulent mixing. Given the sensitivity of the vertical transport to turbulence, developing improved turbulence parameterizations of the stable boundary layer is an important issue.

5. Summary

A mesoscale model and the extensive wind measurements over the Salt Lake valley from a Doppler lidar during the VTMX 2000 field campaign were used to examine the converging slope, canyon, and down-valley flows and their effect on vertical mixing of surface releases. A unique aspect of this study was that the simulated wind fields were transformed into radial velocities so that a direct comparison with lidar measurements could be made. Correlation coefficients between the observed and simulated radial velocities on six constant elevation angles were computed to assess the simulated spatial wind patterns over the valley during eight of the VTMX IOPs. An agreement between the observed and simulated radial velocities was desirable but did not provide a complete evaluation of the predicted winds because a particular radial velocity can be obtained with more than one wind direction. However, the large amount of data (~ 1.3 million data points) over the valley provided an opportunity to evaluate in detail the spatial variations in the simulated wind fields aloft that could not be obtained from point measurements.

The mesoscale model captured reasonably well the general features of the circulations that were observed, including the daytime up-valley flow; the nighttime slope, canyon, and down-valley flows; and the convergence of the flows over the valley. Details of the flows, such as the position and spatial extent of the down-valley and canyon flows, were simulated well during the morning transition period with a high correlation coefficient. The model performance during nocturnal stable conditions was better during evenings with drainage flows modified by synoptic forcing (IOPs 4, 7, and 10) than during evenings with well-developed drainage flows and weak ambient winds aloft (IOPs 5, 6, and 8). The smallest errors in the simulated winds did not occur at the highest altitudes, indicating that the interactions of the valley and ambient winds near the height of the surrounding mountains were not simulated as well as the flows within the valley.

Low correlation coefficients and visual inspections of the spatial wind fields revealed that many of the errors were associated with the timing and structure of specific flows. For example, the simulated transition between up-valley and down-valley flows was usually within 1 h of the observed transition. For some IOPs, the peak down-valley wind speeds were simulated to be 200 m higher than were observed. There were also errors at

times in the location and magnitude of the canyon flows that propagated over the eastern valley, whereas the simulated down-valley flow was consistent with the lidar data. The canyon flows were observed and simulated to advance and retreat over the valley floor several times during the evening, but the variation produced by the model was often out of phase with the lidar measurements. As a consequence, convergence zones were simulated in the right locations but at the wrong times.

In the absence of significant ambient winds aloft, the transition from daytime up-valley and nighttime down-slope flows produced ascending motions over much of the valley between the surface and the height of the surrounding mountains during IOPs 5, 6, and 8. As the down-valley flow gradually developed during the evening regions of descending motions were produced. The average vertical velocity within the valley became close to zero, but ascending vertical motions between 5 and 15 cm s^{-1} occurred where downslope, canyon, and down-valley flows converged. At the base of the Wasatch Mountains and the Traverse Range, ascending vertical motions of greater than 50 cm s^{-1} were produced by hydraulic jumps. For the evenings characterized by significant synoptic forcing (IOPs 4, 7, and 10), ascending motions during the transition period were significantly lower than during IOPs 5, 6, and 8, but after the transition period the magnitudes of the vertical velocities were much higher.

Many of the dispersion characteristics produced by Lagrangian particle model simulations could be classified into three IOP categories: the well-developed drainage circulations, circulations modified by synoptic forcing, and the downslope windstorm events. A fraction of the particles released from the surface was transported up to the height of the surrounding mountains for all three categories, but the vertical distributions were very different among the categories. More particles during the well-developed drainage circulation IOPs were transported to the upper-valley atmosphere between 0.7 and 1.5 km above the valley floor. Sinking motions associated with the near-surface drainage flow trapped surface releases in the stable boundary layer; therefore, the simulations without vertical motions had fewer particles near the surface. Large differences in the particle concentrations occurred between the simulations with and without vertical motions at specific places and times; however, the overall characteristics of the valley atmosphere ventilation differed by about 5%.

The simulation without vertical motions also had a significant number of particles being transported out of the near-surface stable layer to the height of the surrounding mountains. Despite the stability of the valley atmosphere, shear generation of turbulence by the complex flows in the valley was responsible for reducing the number of particles near the ground. The model, however, underestimated TKE aloft when compared with aircraft data, and the upward transport of material may therefore be significantly different than was sim-

ulated. The results demonstrate the importance of reducing uncertainties associated with mesoscale model parameterizations of turbulence.

Acknowledgments. We thank Will Shaw and Kirk Clawson for providing the radar wind profiler data, Bob Banta for his assistance in deploying the Doppler lidar, Brad Orr and Cui-Juan Zhu for their help with the lidar data processing, John Leone for providing the USGS data for the Salt Lake valley, and the reviewers for their constructive comments. This work was supported by the U.S. Department of Energy, under the auspices of the Atmospheric Sciences Program of the Office of Biological and Environmental Research. PNNL is operated for the U.S. DOE by Battelle Memorial Institute.

REFERENCES

- Banta, R. M., L. D. Olivier, W. D. Neff, D. H. Levinson, and D. Ruffieux, 1995: Influence of canyon-induced flows on flow and dispersion over adjacent plains. *Theor. Appl. Climatol.*, **52**, 27–42.
- , and Coauthors, 1997: Nocturnal cleansing flows in a tributary valley. *Atmos. Environ.*, **31**, 2147–2162.
- , L. S. Darby, P. Kaufmann, D. H. Levinson, and C. J. Zhu, 1999: Wind-flow patterns in the Grand Canyon as revealed by Doppler lidar. *J. Appl. Meteor.*, **38**, 1069–1083.
- Chen, C., and W. R. Cotton, 1983: A one-dimensional simulation of the stratocumulus-capped mixed layer. *Bound.-Layer Meteor.*, **25**, 289–321.
- Clark, T. L., W. D. Hall, R. M. Kerr, D. Middleton, L. Radke, F. M. Ralph, P. J. Neiman, and D. Levinson, 2000: Origins of aircraft-damaging clear-air turbulence during the 9 December 1992 Colorado downslope windstorm: Numerical simulations and comparisons with observations. *J. Atmos. Sci.*, **57**, 1105–1131.
- Colle, B. A., and C. F. Mass, 1996: An observational and modeling study of the interaction of low-level southwesterly flow with the Olympic Mountains during COAST IOP 4. *Mon. Wea. Rev.*, **124**, 2152–2175.
- Darby, L. S., R. M. Banta, and R. A. Pielke, 2002: Comparisons between mesoscale model terrain sensitivity studies and Doppler lidar measurements of the sea breeze at Monterey Bay. *Mon. Wea. Rev.*, **130**, 2813–2838.
- Doran, J. C., J. D. Fast, and J. Horel, 2002: The VTMX 2000 campaign. *Bull. Amer. Meteor. Soc.*, **83**, 537–551.
- Fast, J. D., 1995: Mesoscale modeling in areas of highly complex terrain employing a four-dimensional data assimilation technique. *J. Appl. Meteor.*, **34**, 2762–2782.
- , and W. J. Shaw, 2002: Observed and simulated turbulence kinetic energy and dissipation profiles in an urban valley during VTMX 2000. Preprints, *15th Symp. on Boundary Layers and Turbulence*, Wageningen, Netherlands, Amer. Meteor. Soc., 638–641.
- , R. A. Zaveri, X. Bian, E. G. Chapman, and R. C. Easter, 2002: The effect of regional-scale transport on oxidants in the vicinity of Philadelphia during the 1999 NE-OPS field campaign. *J. Geophys. Res.*, **107**, 4307, doi:10.1029/2001JD000980.
- Flamant, C., and Coauthors, 2002: Gap flow in an Alpine valley during a shallow south foehn event: Observations, numerical simulations and hydraulic analogue. *Quart. J. Roy. Meteor. Soc.*, **128**, 1173–1210.
- Helfand, H. M., and J. C. Labraga, 1988: Design of a nonsingular level 2.5 second-order closure model for the prediction of atmospheric turbulence. *J. Atmos. Sci.*, **45**, 113–132.
- Holland, L. D., 2002: Downslope windstorms along the Wasatch Front. M.S. thesis, Dept. of Meteorology, University of Utah, 86 pp.
- Mellor, G. L., and T. Yamada, 1982: Development of a turbulence closure model for geophysical fluid problems. *Rev. Geophys. Space Phys.*, **20**, 851–875.
- Pielke, R. A., and Coauthors, 1992: A comprehensive meteorological modeling system—RAMS. *Meteor. Atmos. Phys.*, **49**, 69–91.
- Reitebuch, O., H. Volkert, C. Wener, A. Dabas, P. Delville, P. Drobinski, P. H. Flamant, and E. Richard, 2003: Determination of airflow across the Alpine ridge by a combination of airborne Doppler lidar, routine radiosounding and numerical simulation. *Quart. J. Roy. Meteor. Soc.*, **129**, 715–727.
- Tremback, C. J., W. A. Lyons, W. P. Thorson, and R. L. Walko, 1994: An emergency response and local weather forecasting software system. Preprints, *Eighth Joint Conf. on the Applications of Air Pollution*, Nashville, TN, Amer. Meteor. Soc., 219–233.
- Zhong, S., and J. D. Fast, 2003: An evaluation of the MM5, RAMS, and Meso-Eta models at subkilometer resolution using VTMX field campaign data in the Salt Lake valley. *Mon. Wea. Rev.*, **131**, 1301–1322.